Chapter 3
Secondary Minerals

Abstract This chapter introduces secondary minerals such as clay minerals, hydroxides and oxides in soils. Clay minerals, which are major secondary minerals in soils, are phyllosilicates that have 1:1 or 2:1 type layers. The 1:1 type minerals are kaolinite and halloysite. The 2:1 type minerals are smectite, vermiculite, micaceous minerals, and chlorite. Gibbsite and manganese oxides are introduced as examples of hydroxides and oxides, respectively. This chapter also constitutes the basic part of treatment of the inorganic constituents in soils. Secondary minerals have an effect on the chemical, physical, and biological functions of soils. As the size of secondary minerals is approximately 2 μm or less, electron micrographs and X-ray diffraction (XRD) are effective for characterizing these minerals. Schematic diagrams are used to interpret the chemical structure of phyllosilicate clay minerals.

3.1 Introduction

The secondary minerals in soil are minerals that are stabilized under various soil environments. The major secondary phyllosilicates in soil are summarized in Table 3.1 with their idealized chemical formulae (Deer et al. 2013). Formula units in association with $O_5(OH)_4$ and $O_{10}(OH)_2$ are also used for 1:1 and 2:1 type phyllosilicate minerals, respectively (Kodama 2012). The major oxides, hydroxides, and other relevant minerals in soil (Kampf et al. 2012) are summarized in Table 3.2. This table includes minerals described in other chapters. Other non-crystalline secondary and primary inorganic materials in soil are described in Chap. 4. These minerals and materials in soil can be altered further if environmental conditions change.

Environmental factors that affect the behavior of secondary minerals include water, temperature, redox condition, biological activities, and time (Churchman and Lowe 2012). In addition, human activities affect secondary minerals and materials through agricultural soil management, civil engineering, and other activities. As examples, the dry–wet cycle affects the shrink–swell behavior of smectitic soils, and the exchangeable cation composition of secondary minerals is easily affected by application of a fertilizer, inundation of seawater, etc. Changes in

Table 3.1 Major secondary phyllosilicate minerals in soil

Secondary phyllosilicate	Chemical formula
Kaolinite	$Al_4Si_4O_{10}(OH)_8$
Halloysite (1.0 nm)	$Al_4Si_4O_{10}(OH)_8 \cdot 4H_2O$
Halloysite (0.7 nm)	$Al_4Si_4O_{10}(OH)_8$
Montmorillonite	$M_{0.67}Si_8(Al_{3.33}Mg_{0.67})O_{20}(OH)_4 \cdot nH_2O$
Beidellite	$M_{0.67}(Si_{7.33}Al_{0.67})Al_4O_{20}(OH)_4 \cdot nH_2O$
Nontronite	$M_{0.67}(Si_{7.33}Al_{0.67})Fe_4O_{20}(OH)_4 \cdot nH_2O$
Vermiculite	$(Mg,Ca)_{0.6-0.9}(Al,Si)_8(Mg,Fe^{3+},Al)_6O_{20}(OH)_4 \cdot nH_2O$
Illite	$K_{1.5-1.0}(Si_{6.5-7.0}Al_{1.5-1.0})\,Al_4O_{20}(OH)_4$
Mg chlorite	$Mg_4Al_2(OH)_{12}(Si_6Al_2)Mg_6O_{20}(OH)_4$

M: Exchangeable cation

Table 3.2 Oxides, hydroxides, and other related inorganic constituents in soil

	Chemical formula
Brucite	$Mg(OH)_2$
Gibbsite	$Al(OH)_3$
Hematite	Fe_2O_3
Goethite	$\alpha\text{-FeOOH}$
Lepidocrosite	$\gamma\text{-FeOOH}$
Ferrihydrite	$Fe_5O_7(OH) \cdot 4H_2O$
Siderite	$FeCO_3$
Lithiophorite	$(Al, Li)MnO_2(OH)_2$
Birnesite	$(Na, Ca)Mn_7O_{14} \cdot 2.8H_2O$
Apatite	$Ca_5(PO_4)_3(F, Cl, OH) \cdot H_2O$
Brushite	$CaHPO_4 \cdot 2H_2O$
Struvite	$MgNH_4PO_4 \cdot 6H_2O$
NH_4-taranakite	$Al_5(NH_4)_3H_6(PO_4)_8 \cdot 18H_2O$
Vivianite	$Fe_3(PO_4)_2 \cdot 8H_2O$
Natrojarosite	$NaFe_3(OH)_6(SO_4)_2$
Gypsum	$CaSO_4 \cdot 2H_2O$
Calcite	$CaCO_3$
Dolomite	$CaMg(CO_3)_2$

redox conditions affect the dissolution and precipitation of iron-bearing minerals and materials. The dissolution and precipitation of iron-bearing minerals and materials is introduced in Chap. 5, and sodification due to seawater inundation is introduced in Sect. 6.2.

Phyllosilicates are the major secondary minerals in soils, and the properties of soils depend on the composition and structure of phyllosilicates. Hence, this chapter begins with the structures of phyllosilicates and then discusses the relationship between the structure and function of phyllosilicates. For identification of phyllosilicates in soil, the changes in basal spacing that occur with changes in exchangeable cations are studied. The basal spacing can be determined with XRD, and changes in the XRD pattern with changes in exchangeable cations (Harris and

White 2008) are shown for several phyllosilicates, with the expectation that these will be helpful for understanding the properties of the phyllosilicates (Molloy and Kerr 1961) as well as scanning electron microscope (SEM) and transmission electron microscope (TEM) images (Sudo and Shimoda 1978).

3.2   Construction of Layer Aluminosilicate Models

The major phyllosilicates of the clay fraction in soil are aluminosilicates. The aluminosilicates are constructed from the phyllosilicate sheet (Fig. 2.3) and the Al octahedral sheet. The octahedral sites of the phyllosilicates may be wholly or partly occupied by Mg or Fe. This section begins with the construction of the Mg octahedral sheet, brucite, followed by the Al octahedral sheet, and the 1:1 type aluminosilicate. Attention is paid to Al–O–Si bonding and the arrangement between the Al octahedral sheet and the Si tetrahedrons of the phyllosilicate sheet. The structure of 1:1 type aluminosilicates to 2:1 types is extended similarly.

3.2.1   Brucite Sheet and Gibbsite Sheet

The construction of the brucite sheet, $Mg(OH)_2$, is shown in Fig. 3.1. On the distant arrangement of blue balls representing OH groups (back OH), small orange-colored balls (Mg) are placed (Fig. 3.1a). The size of the balls roughly indicates the relative
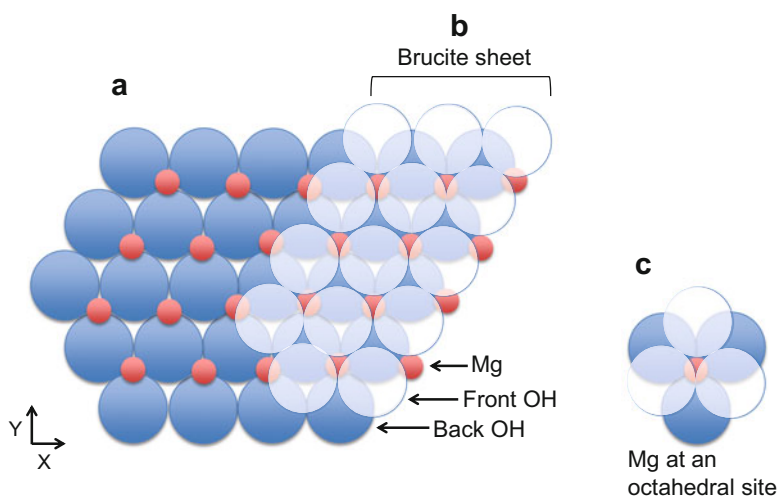

Fig. 3.1 Schematic of a brucite sheet. (**a**) Placement of Mg on back OH groups, (**b**) placement of front OH groups on (**a**) to form a brucite sheet, (**c**) location of Mg at the center of an octahedral site

size of each ion. The procedure of building the sheet is to place three Mg balls alternately among six possible sites around the back OH balls, as shown in Fig. 3.1a. As a result, three Mg sites and three vacant sites are formed around each back OH ball. The front OH balls are placed on the three vacant sites, and the Mg ion is located at the center of an octahedron formed by six OH balls, as shown in Fig. 3.1c. Thus, a brucite sheet is completed (Fig. 3.1b).

3.2.2 Construction of Gibbsite Sheet and 1:1 Layer Aluminosilicate

In the brucite sheet shown in Fig. 3.1, all of the octahedral sites are filled with a Mg ion. In the aluminosilicates, Al ions occupy the octahedral sites instead of Mg ions. Because an Al ion has three positive charges and a Mg ion has two positive charges, one-third of the octahedral sites must be vacant for electroneutrality (Fig. 3.2a). In this way, after two-thirds of the Mg ion sites of the brucite sheet are replaced by Al ions and the remaining Mg ions are removed to make vacant octahedral sites, a gibbsite sheet is formed (Fig. 3.2b).
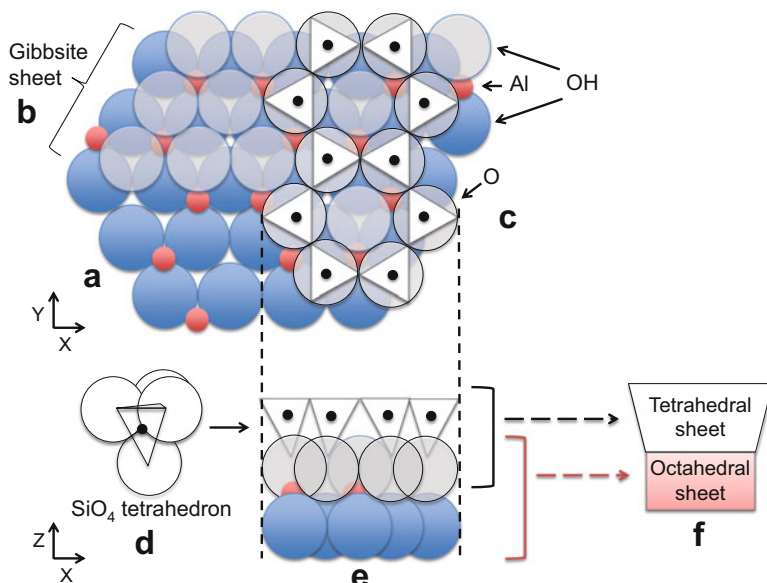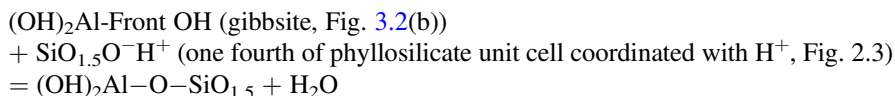

Fig. 3.2 An assembly diagram of a 1:1 dioctahedral aluminosilicate sheet (**a** → **b** → **c**). (**a**) Placement of Al on back OH groups, (**b**) placement of front OH groups to form a gibbsite sheet, (**c**) placement of SiO_4 tetrahedrons onto the front OH groups of the gibbsite sheet, (**d**) location of Si at the center of a tetrahedral site. The SiO_4 group is shown by tetrahedrons (see (**d**)) in (**c**) and (**e**). A horizontal sectional view of (**c**) is shown as (**e**) and further simplification of (**e**) is shown as (**f**)

Connecting a phyllosilicate sheet onto the front OH balls produces a dioctahedral aluminosilicate sheet, as shown in Fig. 3.2c, where Si ions are placed (small black balls) in the center of SiO_4 tetrahedrons (Fig. 3.2d). The reaction of the gibbsite sheet and the phyllosilicate sheet can be formulated simply as

$(OH)_2Al$-Front OH (gibbsite, Fig. 3.2(b))
$+ SiO_{1.5}O^-H^+$ (one fourth of phyllosilicate unit cell coordinated with H^+, Fig. 2.3)
$= (OH)_2Al-O-SiO_{1.5} + H_2O$

where an Al–O–Si bond is formed with the release of a molecule of H_2O (Fig. 3.2e). A front OH group remains at the center of the Si tetrahedron ring (Fig. 3.2c). Further schematic simplification of the tetrahedral and octahedral sheets in Fig. 3.2e gives Fig. 3.2f.

3.2.3   Major Layer Aluminosilicates in Soil

Using the simplification of the tetrahedral sheet and octahedral sheet shown as Fig. 3.2f, the major layer aluminosilicates in soil are represented by six different aluminosilicates in Fig. 3.3. These six layer aluminosilicates can be grouped as 1:1 and 2:1 types. The 1:1 type aluminosilicates have a stacking of one tetrahedral layer and one octahedral layer, whereas the 2:1 type aluminosilicates have an octahedral layer sandwiched by two tetrahedral layers. The major 1:1 type aluminosilicates in soil are kaolinite and halloysite. Halloysite (1.0 nm) has an interlayer of water,
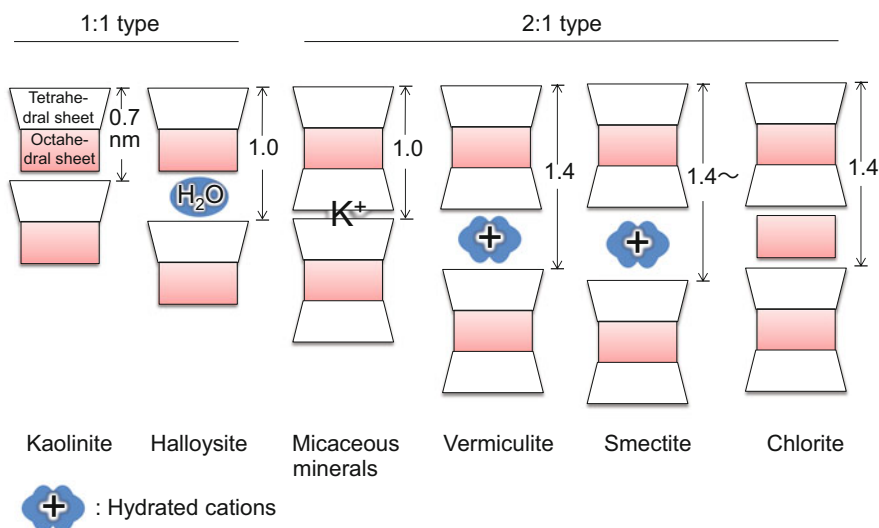

Fig. 3.3 Schematic of phyllosilicate clay minerals. Arrows show basal spacings

whereas halloysite (0.7 nm) does not. The major 2:1 type aluminosilicates are smectite, vermiculite, micaceous minerals, and chlorite.

In layer aluminosilicates, the same unit layer is stacked repeatedly. The distance between one basal plane and the next one, as shown by arrows in Fig. 3.3, is called the basal spacing. The difference in the two halloysites is indicated by the difference in the basal spacing as halloysite (0.7 nm) and halloysite (1.0 nm). The differences among the 2:1 types are characterized by the difference in the basal spacing and changes in the basal spacing that occur with several treatments. The basal spacing of these aluminosilicates is determined by XRD, and the changes in the basal spacing with several treatments (Mg saturation and glyceration, Mg saturation, K saturation, heating at 300 and 550 °C after K saturation, etc.) are used to identify the alumino-silicate clays in soil. As XRD is the most effective tool for identifying the clay mineral composition of soil, XRD patterns are used along with TEM and SEM to introduce clay minerals in the following sections.

As shown in Figs. 3.1 and 3.2, there are two types of octahedral layers. One is the brucite type in which all octahedral sites are occupied by a divalent cation, which is called the trioctahedral type. The other is the gibbsite type, called the dioctahedral type, in which two-thirds of the octahedral sites are occupied by a trivalent cation.

In the secondary minerals in soil, cations in the tetrahedral and octahedral sites are replaced by other cations with similar size and lower valence. This phenomenon is called isomorphous substitution. For example, at the tetrahedral sites, Si^{4+} is partly replaced by Al^{3+}, and at the octahedral sites, Al^{3+} is partly replaced by Mg^{2+} or Fe^{2+}. Although the isomorphous substitution does not affect the crystal structure very much, the number of positive charges decreases and a surplus of negative charge occurs in the aluminosilicate layer. The surplus of negative charge is neutralized by adsorption of cations, called exchangeable cations.

3.2.3.1   1:1 Type Minerals

The 1:1 type minerals include kaolinite and halloysite. A group name of these minerals is "kaolin minerals." Hydrogen bonds connect the 1:1 layers in kaolinite. In the idealized formula (Table 3.1), there is no isomorphic substitution.

Figure 3.4 shows a reference kaolinite sample, kaolinite No. 9 of the American Petroleum Institute (A.P.I.) reference clay minerals. The thin-to-thick platy and partially hexagonal properties of kaolinite minerals can be seen in both the TEM image (Fig. 3.4a) and the SEM image (Fig. 3.4b). XRD patterns of oriented samples show a strong diffraction peak at 0.7 nm, a basal spacing of kaolinite (Fig. 3.3). Although the basal spacing of kaolinite is not affected by the four treatments (Mg saturation and glyceration, Mg saturation, K saturation, and heating at 300 °C after K saturation), kaolin minerals are converted to an amorphous state by heating at 550 °C, and the diffraction peak at 0.7 nm disappears (Fig. 3.4c).

Kaolinite is one of the most frequently found clay minerals in soil. Figure 3.5 shows an example from the Bt2 horizon of an Ultic Palexeralf used for a vineyard in Nuble Province, Chile. The TEM image (Fig. 3.5c) and SEM image (Fig. 3.5d) show
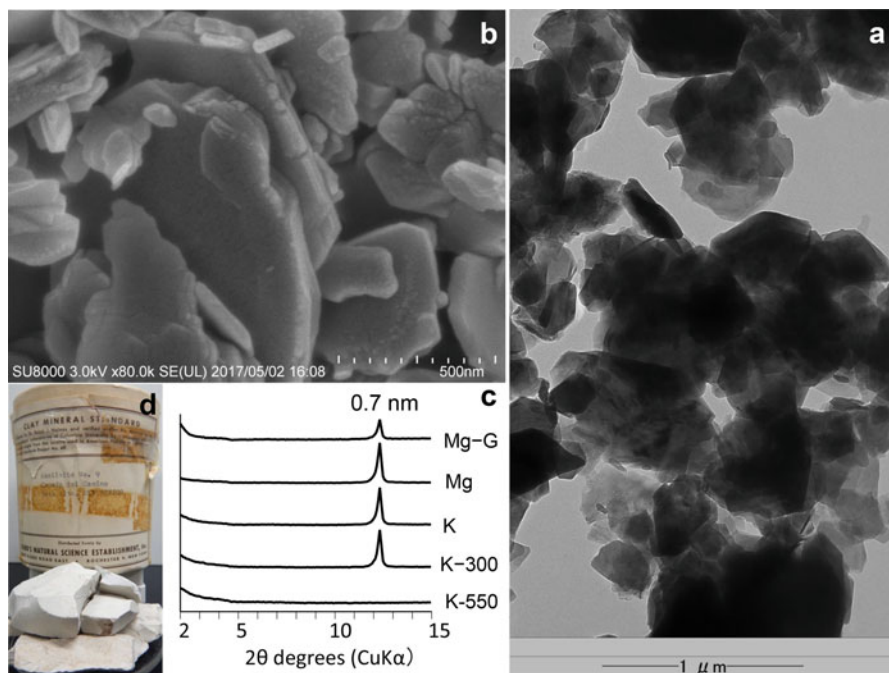
Fig. 3.4 Reference sample of kaolinite. (**a**) TEM image, (**b**) SEM image, and (**c**) XRD patterns with five treatments (Mg saturation with glyceration, Mg saturation, K saturation, heating at 300 °C after K saturation, and heating at 550 °C after K saturation) of the oriented clay fraction, (**d**) dried clods of the reference kaolinite

smaller and more sub-round platy particles than those in Fig. 3.4. The XRD patterns of the kaolinite in Fig. 3.5e show the major diffraction peak at 0.7 nm, the basal spacing of kaolinite, and are basically the same as those in Fig. 3.4c. However, the 0.7 nm diffraction peak is broader than the peak in Fig. 3.4c, which suggests lower crystallinity of the kaolinite in Fig. 3.5 compared with the kaolinite in Fig. 3.4. A small amount of 2:1 clay mineral, suggested by the diffraction peaks at 1.4 nm (Mg saturation) and 1.0 nm (K saturation, heating at 300 °C after K saturation, and heating at 550 °C after K saturation) is also indicated in Fig. 3.5e.

Kaolinite is the major clay mineral of Oxisols, Ultisols, and other soils. The cation exchange capacity (CEC) of kaolinite is typically less than 10 $cmol_c$ kg^{-1}, and it characterizes the oxic horizon and Oxisols in the Soil Taxonomy of the United States Department of Agriculture (Soil Survey Staff 1999). Weatherable minerals in Oxisols are so limited that Oxisols are considered highly weathered soils. Thus, kaolinite is the most weathered member of the layer aluminosilicates in soil. Oxisols are distributed in central Africa and Brazil with tropical rainforest climate. They occupy about 12% of the world's soils.

Halloysite, the other major member of the 1:1 type minerals, is found in many soils as a major or minor component of the clay fraction. Halloysite also occurs in
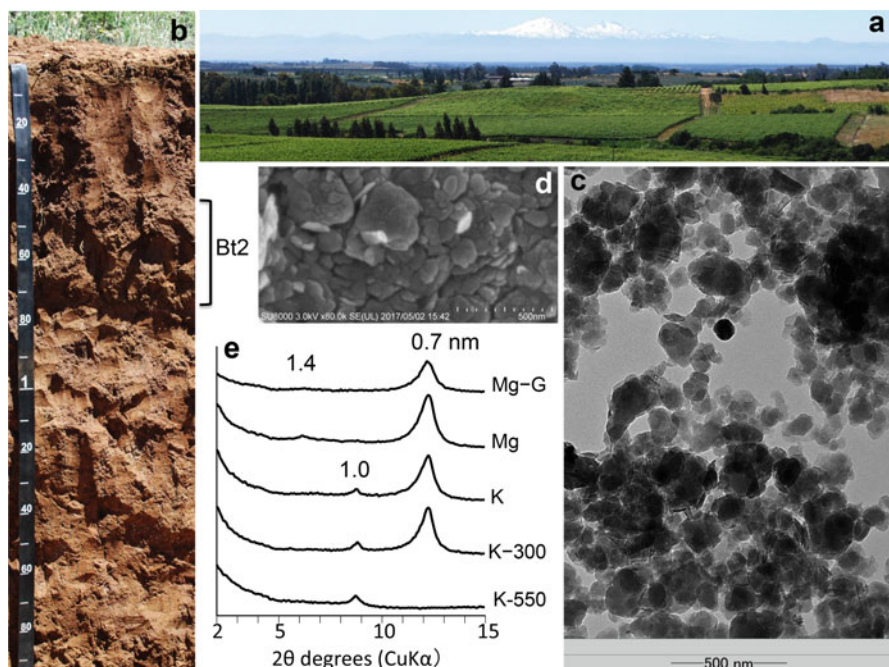
Fig. 3.5 Kaolinite in soil. (**a**) Landscape, (**b**) soil profile with kaolinite-rich soil horizons. A kaolinite-rich clay fraction was prepared from the Bt2 horizon (**b**). (**c**) TEM image, (**d**) SEM image, (**e**) XRD patterns with five treatments (Mg saturation with glyceration, Mg saturation, K saturation, heating at 300 °C after K saturation, and heating at 550 °C after K saturation) of the dithionite–citrate–bicarbonate treated and oriented clay fraction

Andisols under semi-dry climates and in the lower horizons of Andisols under humid climate. Figure 3.6 shows an example of a halloysite-containing, partially weathered volcanic ash in the lower horizon (2C2) of a soil in Aizu, Japan. A possible reason for the halloysite formation from volcanic ash is the poor drainage of this area.

The morphological and chemical properties of halloysite are diverse. Halloysite shows thin platy, curved tubular, and spherically curved properties under TEM observation (Fig. 3.6b). There are two types of halloysite, halloysite (1.0 nm) and halloysite (0.7 nm). The values in parentheses indicate their basal spacing. XRD patterns are effective for distinguishing the two types of halloysite. Glyceration causes its basal spacing to expand to 1.1 nm, and the basal spacing of halloysite (1.0 nm) decreases to 0.7 nm with heating at 300 °C (Fig. 3.6c). The 0.7 nm basal spacing of kaolinite and halloysite disappear with heating at 550 °C because these clays are converted to a non-crystalline phase. The CEC of halloysite ranges up to 40 $cmol_c$ kg^{-1}, and some halloysites show high selectivity for K^+ and NH_4^+.

Kaolin minerals were described in detail by Dixon (1989). Recently, halloysite was reviewed by Joussein et al. (2005) and by Churchman et al. (2016).
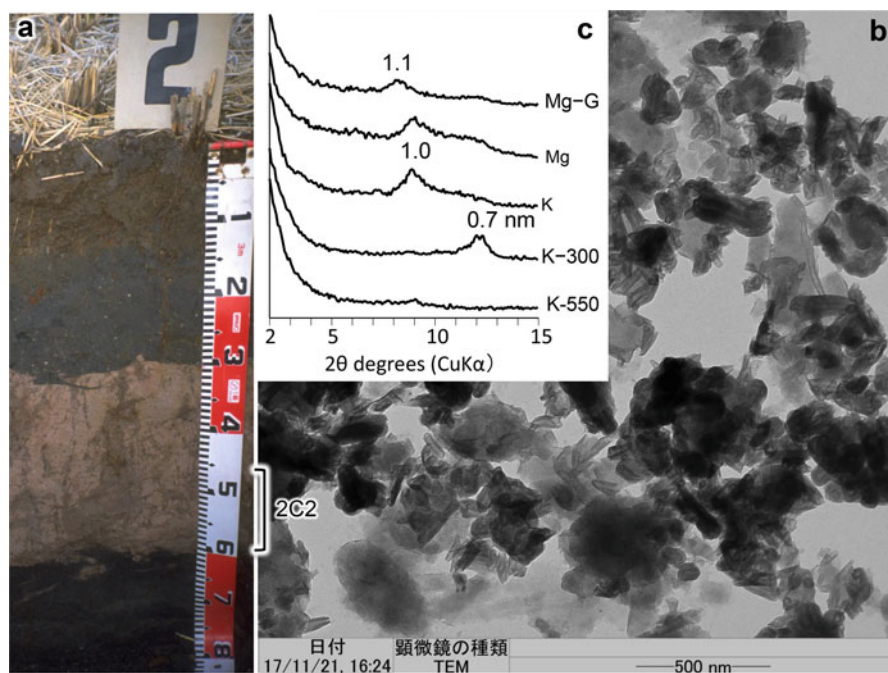
Fig. 3.6 Halloysite in partially weathered volcanic ash horizons. (**a**) A soil profile. A kaolin-rich clay fraction was prepared from the 2C2 horizon. (**b**) TEM image, (**c**) XRD patterns with five treatments (Mg saturation with glyceration, Mg saturation, K saturation, heating at 300 °C after K saturation, and heating at 550 °C after K saturation) of the dithionite–citrate–bicarbonate treated and oriented clay fraction

3.2.3.2   2:1 Type Minerals

Major 2:1 type minerals include smectite, vermiculite, micaceous minerals, chlorite, etc. (Table 3.1, Fig. 3.3). Among these minerals, smectite and vermiculite show high CEC, ranging between 90 and 150 $cmol_c\ kg^{-1}$. Soils having these clay minerals and neutral-range pH are fertile because the minerals can carry a large amount of nutrient cations due to their high CEC.

Smectite is a group name including three members, montmorillonite, beidellite, and nontronite. The differences of the members are the major site of isomorphous substitution and the ions at the sites of substitution. Montmorillonite has major isomorphous substitution at the octahedral sites, whereas beidellite has it at the tetrahedral sites. Montmorillonite can be distinguished from other smectites by using the Greene-Kelly test (Greene-Kelly 1955; Mala and Douglas 1987). If beidellite has a large amount of iron at the octahedral sites, it is called nontronite (Table 3.1).

Smectite looks like thin sheets. Figure 3.7a, a TEM image of a reference smectite, suggests that many thin smectite sheets are randomly overlapped. Figure 3.7b, an
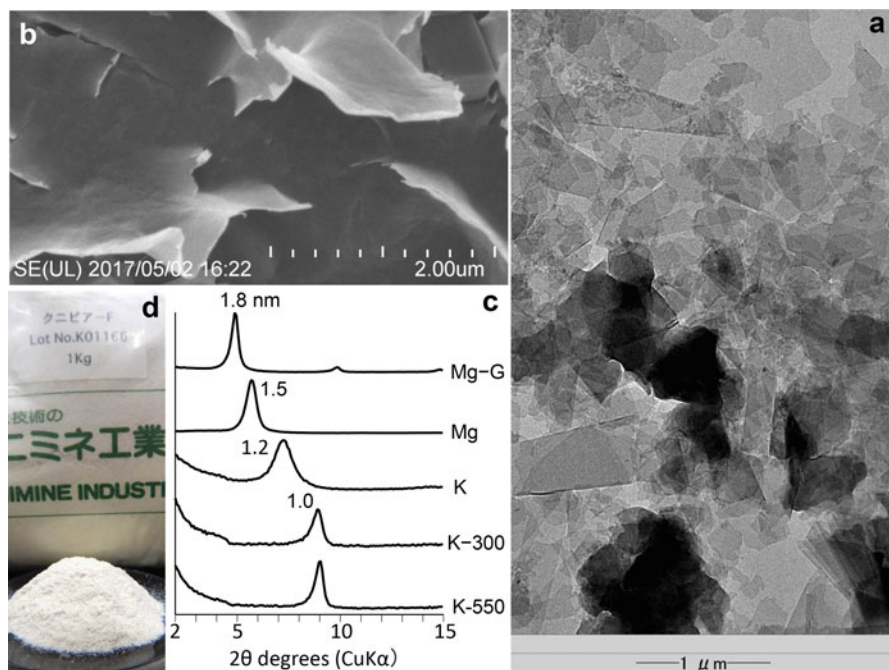
Fig. 3.7 Reference montmorillonite. (**a**) TEM image, (**b**) SEM image, (**c**) XRD patterns of the oriented clay fraction of Kunipia F (**d**) with five treatments (Mg saturation with glyceration, Mg saturation, K saturation, heating at 300 °C after K saturation, and heating at 550 °C after K saturation). Kunipia F, is natural montmorillonite produced at Tsukinuno, Yamagata Prefecture, Japan

SEM image showing the surface of the overlapped sheets, suggests that some thin sheets are turned up.

The basal spacing of smectite expands to accommodate water or organic compounds in the interlayer sites. In other words, the smectite swells. When the exchangeable cation is Mg^{2+}, the basal spacing is 1.4–1.5 nm (Fig. 3.7c), which is due to the six-coordination of water molecules around a divalent cation. The arrangement of six water molecules corresponds to two layers of water molecules at the interlayer site. The basal spacing of Mg^{2+}-saturated smectite (1.5 nm) expands to 1.8 nm with the treatment by glycerin. This property is used to identify smectite in soil.

Similar electron micrographs are obtained from smectite-rich soil (Fig. 3.8). The TEM image (Fig. 3.7a) shows overlapped thin sheets, and the SEM image suggests turned up thin sheets (Fig. 3.7b). The XRD peaks for the basal spacing are broader than those in Fig. 3.7c. A small diffraction peak at 0.7 nm (Fig. 3.8c) is probably from kaolinite, a minor component of this clay fraction.

Montmorillonite shows higher swelling than the other two members of the smectite group (Greene-Kelly 1955; Egashira and Ohtsubo 1983). Both smectites,
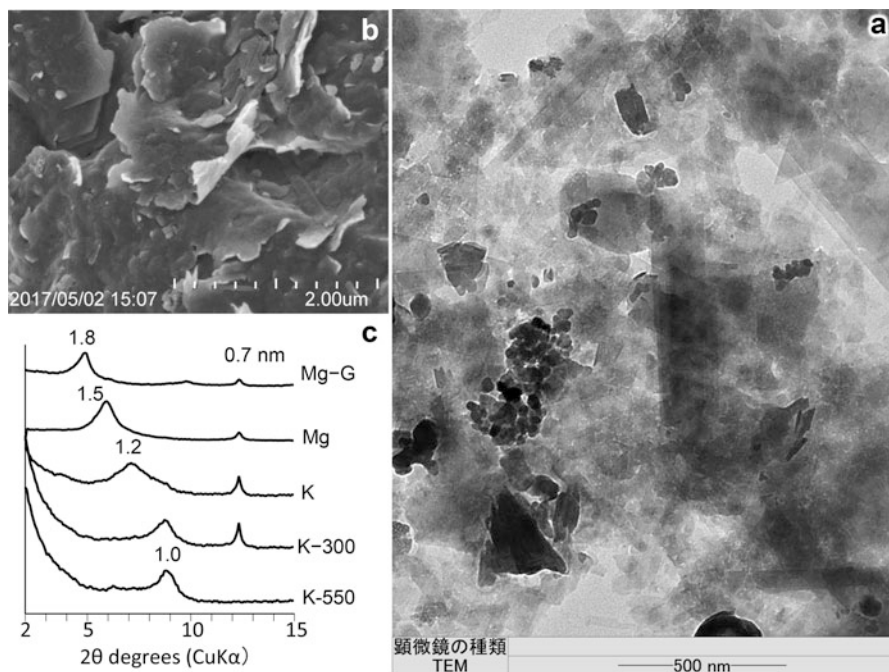
Fig. 3.8 Montmorillonite from subsoil of a paddy field. (**a**) TEM image, (**b**) SEM image, (**c**) XRD patterns with five treatments (Mg saturation with glyceration, Mg saturation, K saturation, heating at 300 °C after K saturation, and heating at 550 °C after K saturation) of the dithionite–citrate–bicarbonate treated, and oriented clay fraction. The clay fraction was obtained from the 25–40 cm horizon (Bg2) of the pedon shown in Fig. 5.22b

Figs. 3.7 and 3.8, are montmorillonite because the basal spacing is about 0.98 nm by the Greene-Kelly test (Li$^+$ saturation, heating at 250 °C, and glyceration). Montmorillonite has a greater amount of isomorphous substitution at the octahedral sites than the other smectites. The layer charge of montmorillonite is diminished by Li$^+$, which can possibly penetrate into the cation deficient octahedral sites due to its small ionic size. As a result, the swelling property of montmorillonite is diminished. When it is saturated with K$^+$ and heated at 300 °C followed by glyceration, the basal spacing expands to 1.8 nm, which is also a property of montmorillonite (Malla and Douglas 1987).

Soils with abundant smectite show an intensive shrink–swell cycle under semi-dry climate, in which a dry season alternates with a wet season. In the dry season, wide cracks form from the soil surface to a depth of several tens of cm or deeper. The cracks may develop horizontally or diagonally, not only vertically. When the rainy season begins, water enters the lower horizons of the soil along the cracks and swelling begins at all sites having moisture. The swelling force at the lower horizon may lift the upper soil, and the soil horizon may become undulated. Uneven swelling at the lower horizon makes a sliding surface in the soil, a slickenside. These are the

properties of Vertisols, which occupy about 3% of the world's soil and are distributed mainly in a portion of the Mexico Gulf region, a part of India, the upper Nile flow region, and southeastern Australia. Without alternating wet and dry seasons, Vertisols do not form even if smectite is abundant in the soil.

The characteristics of vermiculite are high CEC, dominance of the trioctahedral type, and a wide range of particle size from sand to clay. The basal spacing of Mg^{2+}-saturated vermiculite is 1.4 nm. The spacing decreases to 1.0 nm with K^+ saturation, and it does not expand with glyceration. This property is used to identify vermiculite in soil from XRD patterns. The trioctahedral vermiculite can form from trioctahedral micas in a tephra-deived soil (Nanzyo et al. 2001).

Figure 3.9 shows the TEM image, SEM image, and XRD patterns of the clay fraction prepared from the Bw horizon of the soil profile shown in Fig. 6.24. The TEM image (Fig. 3.9a) suggests that this clay fraction has mixed clay minerals. The major ones are vermiculite (platy) and halloysite (curved tubular).

One of the minimal swelling members of the 2:1 minerals is micaceous minerals (Fig. 3.3) including illite (Table 3.1). The basal spacing of micaceous minerals is 1.0 nm, and the basal spacing hardly changes with heating at 300 or 550 °C. Negative charges of the aluminosilicate layer are neutralized with K^+, which is fixed in the interlayer site. The interlayer K^+ is exchanged little with other cations.
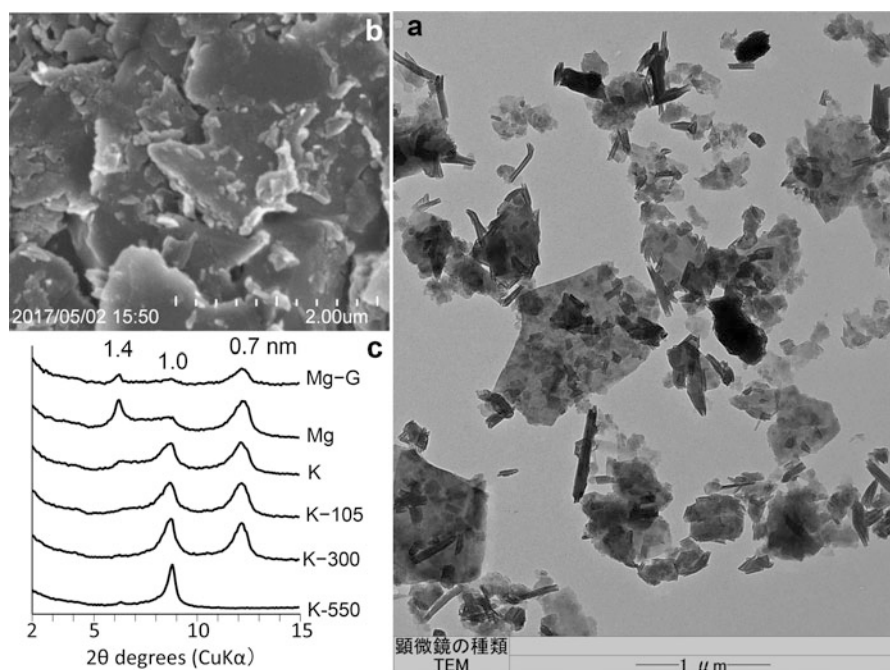

Fig. 3.9 The Clay fraction obtained from 7–22 cm horizon (Bw) of the pedon shown in Fig. 6.24. (**a**) TEM image, (**b**) SEM image, (**c**) XRD patterns with six treatments (Mg saturation with glyceration, Mg saturation, K saturation, and heating at 105, 300, and 550 °C after K saturation, respectively) of the oriented vermiculite-containing clay fraction

The particle size of micaceous minerals ranges widely between sand Figs. 2.10 and 2.11 and clay. Micaceous minerals are also formed by diagenesis, not only from the weathering of igneous rocks.

The final member of the 2:1 minerals is chlorite (Fig. 3.3). Chlorite has an inorganic polymer at the interlayer site. For example, in Mg chlorite (Table 3.1), negative charges of the aluminosilicate layer accommodate a positively charged brucite layer in which Mg^{2+} is partly replaced with Al^{3+}. Chlorite can be regarded as a 2:1:1 type mineral, in which the last layer is, for example, the brucite layer of Mg chlorite.

As an example of chlorite, a clay fraction prepared from partially weathered chlorite schist (metamorphic rock) is shown in Figs. 3.10a, b. As shown in the SEM image (Fig. 3.10b) of the clay fraction, chlorite is also thin plates, but these plates are thicker than those of smectite. The basal spacing of chlorite is 1.4 nm (Fig. 3.3). Although this basal spacing is not affected by Mg^{2+} or K^+ saturation, the peak intensity of the 1.4 nm reflection increases with heating at 550 °C (Fig. 3.10c).

In acid soils, types intermediate between vermiculite (or smectite) and chlorite are often found. These are chloritized vermiculite and chloritized smectite. These
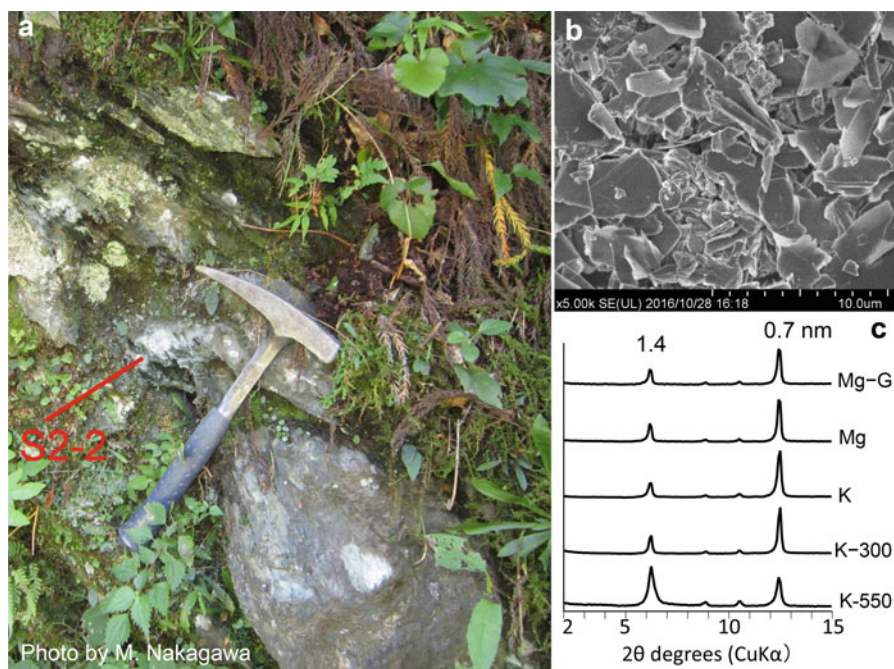

Fig. 3.10 (**a**) Partially weathered chlorite schist, (**b**) SEM image of the chlorite-rich clay fraction prepared from the position S2–2 of (**a**), (**c**) XRD patterns with five treatments (Mg saturation with glyceration, Mg saturation, K saturation, heating at 300 °C after K saturation, and heating at 550 °C after K saturation) of the oriented clay fraction. The chlorite schist was sampled near the boundary between the chlorite and gabbro zones along the Asemi-gawa River (Higashino 1990; Taguchi and Enami 2014) by M. Nakagawa

minerals appear to form through polymerization of exchangeable Al in an acid soil, but the polymerization of Al is not complete as in a gibbsite sheet. The position of the XRD peak of the basal spacing appears broadly between 1.4 and 1.0 nm after heating at 300 °C. Several researchers have used citrate, fluoride, etc., to remove the polymerized Al interlayering (Barnhisel 1977).

Acid soils, soils with pH(H_2O) roughly less than 5.5, have exchangeable or KCl-extractable Al and cause Al-overload disorders in sensitive plants. Liming is effective for removing this exchangeable Al. Further, application of other plant nutrients, such as Mg, K, P, etc., is necessary to improve crop production in acid soils.

3.2.4   Dioctahedral and Trioctahedral Type

The difference in the octahedral layers between dioctahedral and trioctahedral types appears to affect the weathering resistance of 2:1 type aluminosilicates. By comparing the muscovite and the weathered biotite in Fig. 2.9, biotite appears to weather earlier than muscovite in soil. The octahedral layer of biotite is the trioctahedral type, and that of muscovite is the dioctahedral type.

Figure 3.11 schematically shows the differences between trioctahedral and dioctahedral micas. Potassium ion locates at the center of two six-membered Si tetrahedron rings and is sandwiched by both upper and lower phyllosilicate layers, as shown in Fig. 3.11a, b. In the trioctahedral type, through observation of the lower aluminosilicate shown in Fig. 3.11a from the plane shown in Fig. 3.11c, the six-membered Si tetrahedron ring and a part of the lower trioctahedral layer appear (Fig. 3.11d). At the center of the Si tetrahedron ring, there is a front OH. The direction of the proton of the front OH is perpendicular to the phyllosilicate plane because the front OH is surrounded by three Al ions. Due to the difference in electronegativity between O and H, the H is positively charged slightly. Hence, a repulsive force occurs between K^+ and $H^{\delta+}$. On the other hand, in the dioctahedral type, one-third of the octahedral sites are vacant, and the proton of the front OH can be directed to the vacant octahedral site (Fig. 3.11e). Returning to Fig. 3.11a, b, the repulsion between K^+ and $H^{\delta+}$ is weaker in the dioctahedral type than in the trioctahedral type. This is the possible reason why dioctahedral mica is more stable than trioctahedral mica in soil.

The position of the powder XRD peak of the (060) plane can be used to distinguish the trioctahedral type from the dioctahedral type. The positions of the XRD peak of these two types are 1.53 and 1.50 nm, respectively. If a clay sample is a mixture of the two types, it is difficult to make this distinction. When the mixture is with kaolin minerals, peaks from the kaolin minerals can be removed by heating at 550 °C. If the composition of the remaining mineral is simple enough, distinction between these two types using the position of the (060) peak may be possible (Nanzyo et al. 2001).
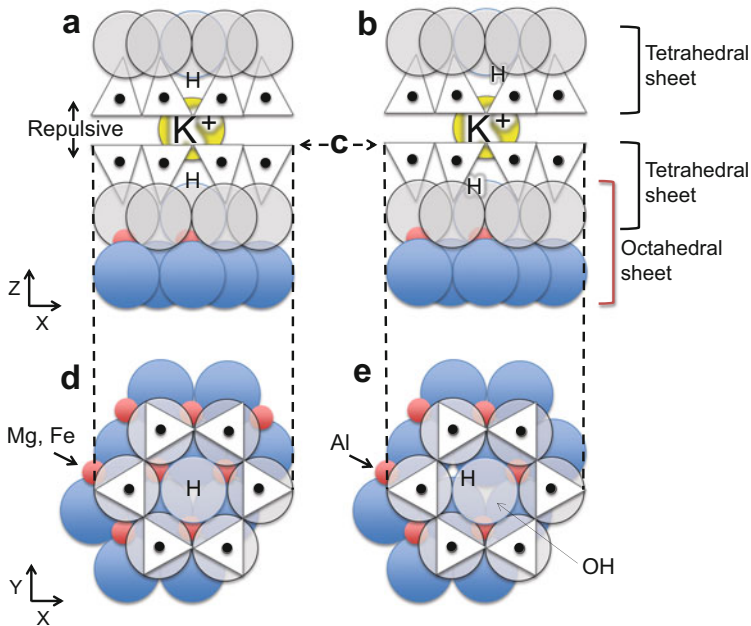
Fig. 3.11 Schematic showing the differences between biotite (left) and muscovite (right). (**a** and **b**) Potassium ion sandwiched by both upper and lower phyllosilicate layers, (**c**) the plane to show the lower aluminosilicate (**d** and **e**)

3.3 Oxides, Hydroxides, and Others

Secondary minerals in soil other than phyllosilicates include oxides, hydroxides, carbonates, sulfates, phosphates, halides, etc., and these are summarized in Table 3.2. Some of these are reaction products between soil inorganic constituents and fertilizers added to farmland. In this section, gibbsite and manganese oxides are considered. The minerals in Table 3.2 include minerals introduced in subsequent chapters.

Gibbsite

Gibbsite is an aluminum hydroxide [Al(OH)$_3$] mineral occurring in highly weathered soils such as Oxisols (Hsu 1989). The gibbsite sheet was shown in Fig. 3.2b. Gibbsite sheets stack in the Z direction with hydrogen bonding.

Gibbsite also occurs in Andisols (Wada and Aomine 1966). Figure 3.12a, b shows an Andisol having a gibbsite-containing horizon at the depth of 66–85 cm from the surface. Gibbsite exists in the 0.2–0.05, 0.05–0.02, and 0.02–0.005 mm particle size fractions as shown by the XRD peaks at the d-spacing of 0.485 and 0.437 nm.

In the 0.05–0.02 mm particle size fraction, gibbsite particles were found using element mapping; they appear as Al-rich particles. In Fig. 3.13, there are two
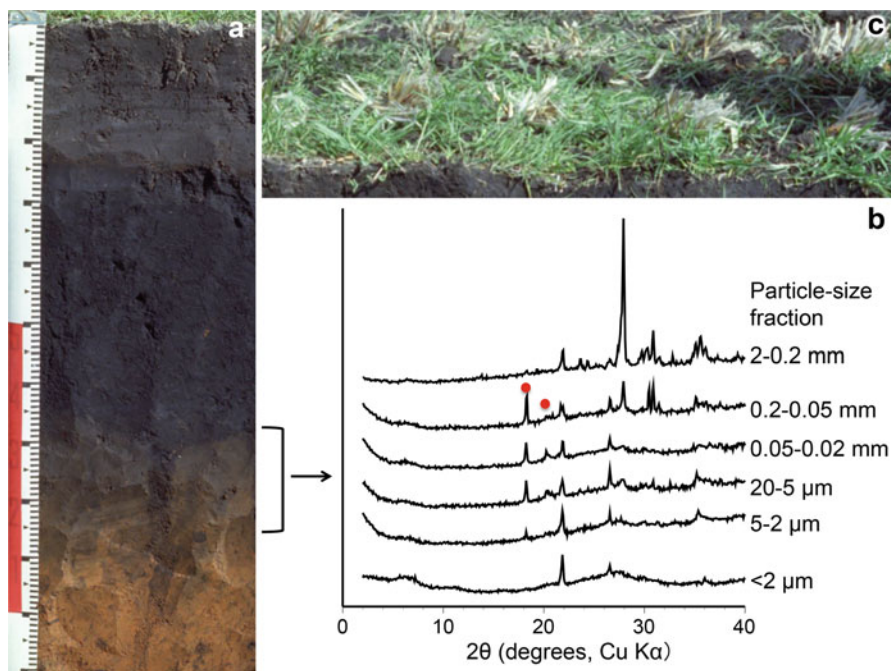
Fig. 3.12 Preparation of a gibbsite sample. (**a**) An Andisol profile having a gibbsite-containing horizon at the depth of 66–85 cm, (**b**) XRD patterns of six particle size fractions of the gibbsite-containing soil horizon, (**c**) the present land use (paddy field, after harvest). Red closed circles indicate the highest (d = 0.485 nm) and second highest (d = 0.437 nm) XRD peaks of gibbsite

gibbsite particles marked by the letters (a) and (b). As shown by the EDX spectra (Fig. 3.13a, b), the cations of these particles are mostly Al. Other particles in Fig. 3.13 are aggregates of allophanic non-crystalline materials (most abundant, Fig. 3.13c) and non-colored volcanic glass (Fig. 3.13d). Because allophanic materials and volcanic glass show no sharp XRD peaks, the 0.485 nm peak from gibbsite appears as the highest peak in the 0.05–0.02 mm fraction (Fig. 3.12b). It is deducible that with intensive leaching of Si, Ca, Na, etc., from volcanic glass, Al-rich particles such as allophanic materials and gibbsite formed.

Gibbsite particles appear to have hexagonal platy characteristics (Hsu 1989). Figure 3.14 is the magnified SEM image of the particle (b) shown in Fig. 3.13. The lower part of the particle shown in Fig. 3.14 has hexagonal platy characteristics.

Manganese Oxides and Hydroxides

Manganese is one of the major elements in soil and also one of the essential elements for plants, animals, and other organisms. Macroscopically, manganese oxides and hydroxides appear in soil as nodules. Small patchy concentrated manganese is sometimes found in the subsoil of irrigation water paddy field. However, it is not easy to separate manganese minerals unless they are not concentrated as nodules or concretions.
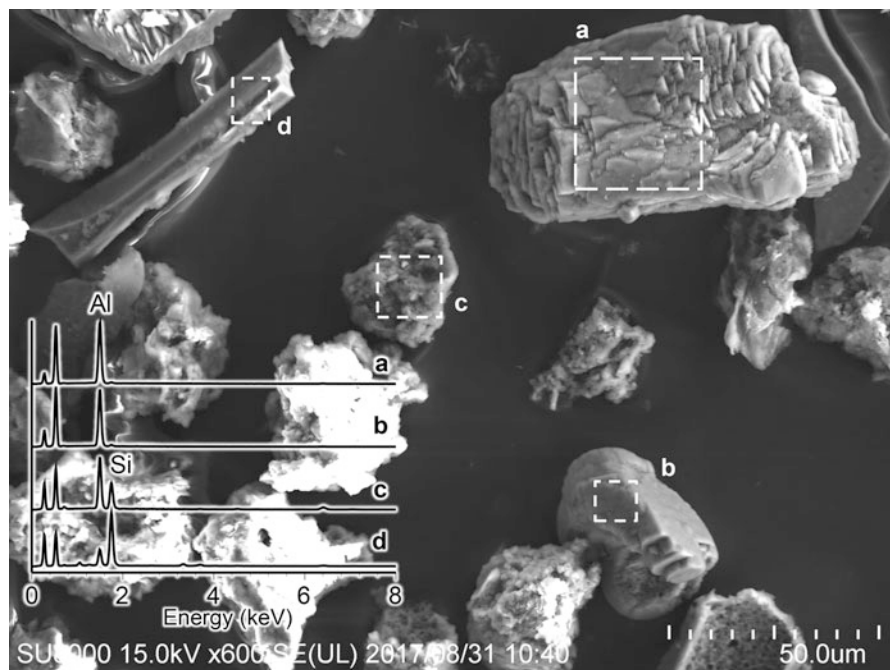
Fig. 3.13 SEM image of the 0.05–0.02 mm fraction of the gibbsite-containing soil horizon at the depth of 66–85 cm of the pedon shown in Fig. 3.12a. EDX spectra (**a**), (**b**), (**c**), and (**d**) were obtained from the dashed areas (**a**), (**b**), (**c**), and (**d**) of the different particles, respectively
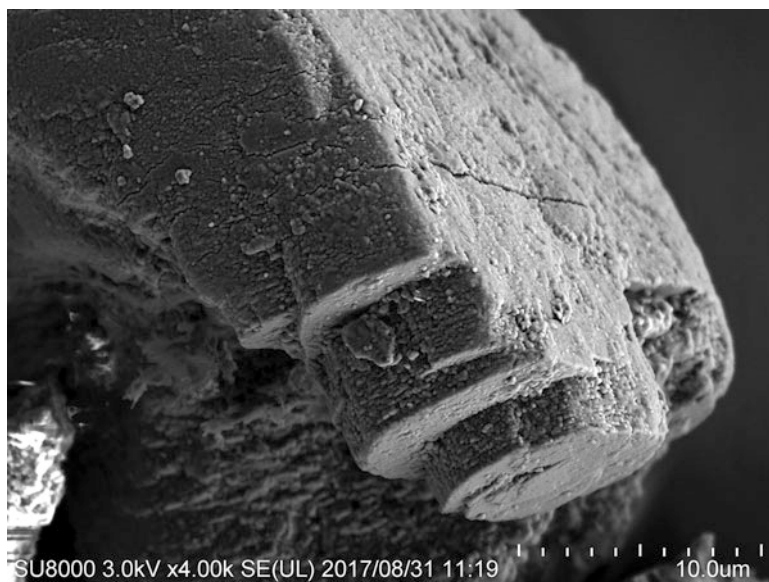

Fig. 3.14 Magnified SEM image of the gibbsite particle labeled as Fig. 3.13b

From among the manganese minerals reviewed by McKenzie (1989), the examples of birnesite and lithiophorite are introduced in this section. Birnesite is a group of manganese oxides including δ-MnO_2, manganous manganite, and others. According to McKenzie (1989), the birnesite group is characterized by a 0.7 nm XRD basal reflection and its higher order. The chemical formula of lithiophorite is $(Al,Li)MnO_2(OH)_2$. Analyses of lithiophorite and birnesite show high Mn_3O_4 concentration (McKenzie 1989).

Manganese nodules were collected from the soil surface of Yomitan-son, Okinawa Prefecture, Japan (Fig. 3.15a, b) by hand-picking. The Mn nodules are dark-colored balls with a diameter of about 1 cm (Fig. 3.15b). Tokashiki et al. (2003) used a sequential selective dissolution method to separate the birnesite, lithiophorite, and also goethite in soil manganese nodules. X-ray diffraction patterns were used to confirm the presence of these minerals. To obtain visual information for these manganese minerals, polished sections of the Mn nodules (Fig. 3.15c) were prepared. Following the sequential selective dissolution method of Tokashiki et al. (2003), a small diffraction peak at 0.72 nm (Fig. 3.15d), which appeared after 5 M
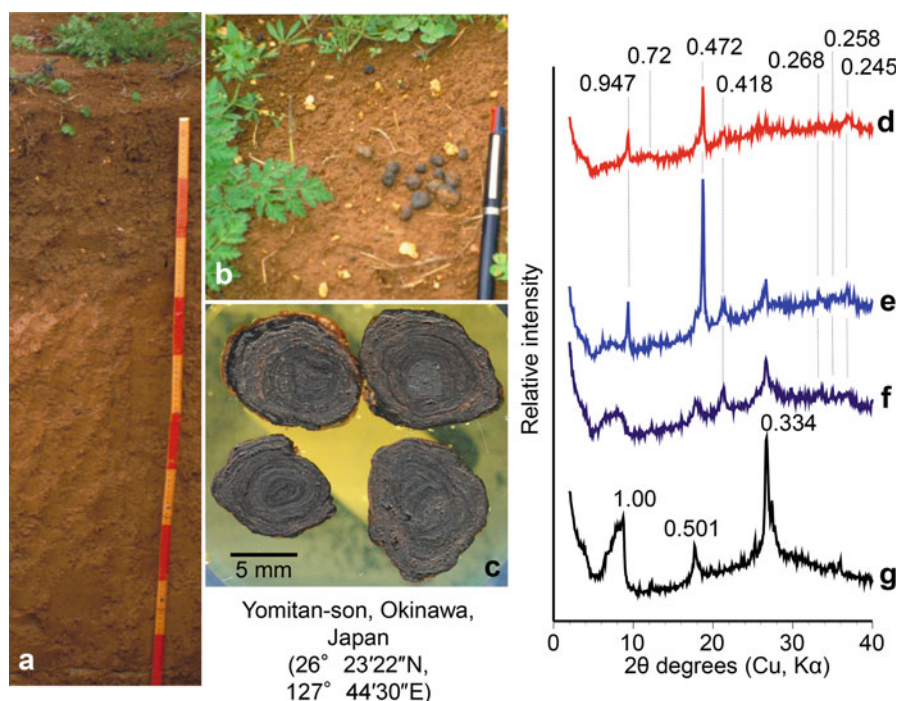

Fig. 3.15 (**a**) Soil profile, (**b**) manganese nodules collected from the surface of soil (**a**), (**c**) polished section of the manganese nodules, (**d, e, f**, and **g**) XRD patterns with four sequential treatments of the ground manganese nodules (**d**: after 5 M NaOH treatment, **e**: after hydroxyl amine hydrochloride treatment (HAHC) at 25 °C, **f**: after HAHC at 60 °C, **g**: after dithionite–citrate–bicarbonate treatment). The XRD patterns were obtained by air-drying a sample suspension on a slide glass

NaOH treatment of powdered Mn nodule and disappeared after hydroxylamine hydrochloride treatment (HAHC) at 25 °C, suggests birnesite. The intensity of diffraction peaks at 0.947 and 0.472 nm increased with the HAHC treatment at 25 °C and disappeared with the HAHC treatment at 60 °C, suggesting lithiophorite. The intensity of diffraction peaks at 0.418, 0.268, 0.258, and 0.245 nm, which disappeared with dithionite–citrate–bicarbonate (DCB), suggests goethite. The diffraction peaks that remained after the DCB treatment, 1.00, 0.501, and 0.334 nm, correspond to those of a micaceous mineral. All of these results are close to those reported by Tokashiki et al. (2003).

In the optical micrograph (Fig. 3.16a) of a polished section, concentric color distribution patterns of brown and dark - gray can be seen. By comparing the optical photograph (Fig. 3.16a) with the Fe element map (Fig. 3.16b), the brown color can be approximately correlated with iron concentration. Among these concentric color and iron distribution patterns, Mn concentration is higher in the dark - gray parts (Fig. 3.16d) than in the brown iron-rich parts (Fig. 3.16c, e). In the magnified Mn element map (Fig. 3.16f) of the dashed square in Fig. 3.16a, Mn-concentrated spots occur in the lower-right dashed square.
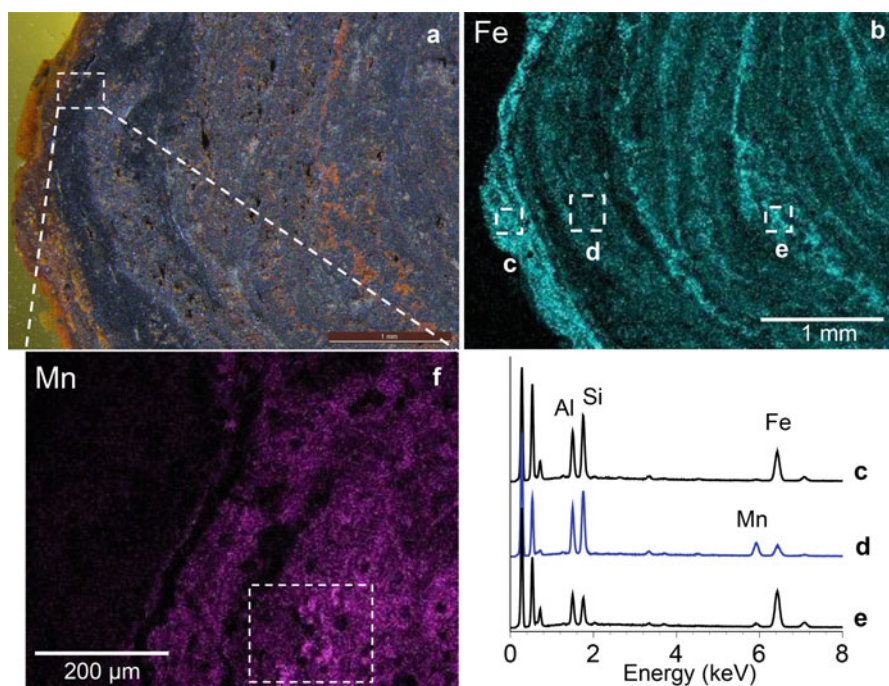

Fig. 3.16 EDX analyses of a manganese nodule. (**a**) Optical photograph of polished section showing a magnified view of the left-hand side of the upper left nodule in Fig. 3.15c, (**b**) an element map showing Fe distribution of (**a**), (**c, d,** and **e**) EDX spectra obtained from the dashed squares (**c**), (**d**) and (**e**) in (**b**), (**f**) a magnified element map showing Mn distribution of the dashed square in (**a**)
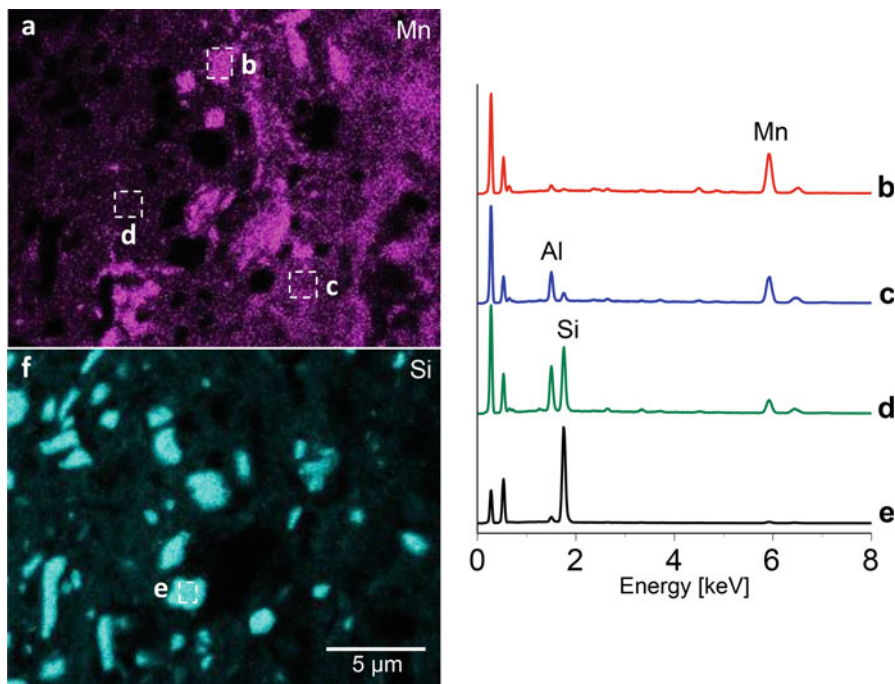
Fig. 3.17 EDX analyses with higher magnification. (**a**) magnified element map of Mn of the dashed square in Fig. 3.16f, (**b, c**, and **d**) EDX spectra obtained from the dashed squares (**b**), (**c**), and (**d**) in (**a**), (**e**) EDX spectrum obtained from the dashed square (**e**) in the Si element map (**f**) of the same area as in (**a**)

Further magnification of the dashed square in Fig. 3.16f gave Fig. 3.17a, in which different Mn concentration areas can be found. In the highest Mn concentration areas, for example the dashed square (b), the concentration of Mn is much higher than the concentration of other elements, as shown in the EDX spectrum shown in Fig. 3.17b. In the second-highest Mn concentration areas, for example the dashed area (c), Mn and Al concentrations are high, as shown in the EDX spectrum shown in Fig. 3.17c. In the third-highest Mn concentration areas, for example the dashed area (d), Si and Al concentrations are much higher than Mn concentration, as shown by the EDX spectrum shown in Fig. 3.17d. In the lowest Mn concentration areas, Si concentration is high, as shown by the Si element map (Fig. 3.17f) and the EDX spectrum shown in Fig. 3.17e. Considering the analyses of manganese minerals (Mn_3O_4: 83.2 and 73.2%; Al_2O_3: 1.0 and 11.5% for birrnessite and lithiophorite, respectively (McKenzie 1989)) and the results from the sequential selective dissolution analyses (Fig. 3.15), the major component of the dashed areas shown in Fig. 3.17b, c can be related to birnesite and lithiophorite, respectively. The major components of the areas of the EDX spectra shown in Fig. 3.17d, e can be related to a dioctahedral micaceous mineral (Fig. 3.15g) and fine silica particles, respectively.

As suggested by the small peaks in EDX spectra (b), (c), (d), and (e), those dashed areas in Fig. 3.17a, f may be a mixture with other minor components.

Further readings for this chapter are Dixon and Weed (1989) and Dixon and Schulze (2002).

References

Barnhisel RI (1977) Chlorites and hydroxyl interlayered vermiculite and smectite. In: Dixon JB, Weed SB, Kttrick JA, Milford MH, White JL (eds) Minerals in soil environment. SSSA, Madison

Churchman GJ, Lowe DJ (2012) Alteration, formation, and occurrence of minerals in soils. In: Huang PM, Li Y, Sumner ME (eds) Handbook of soil sciences, properties and processes, vol 20, 2nd edn. CRC Press/Taylor & Francis Group, Boca Raton/London/New York, pp 1–72

Churchman GJ, Pasbakhsh P, Hillier S (2016) The rise and rise of halloysite. Clay Miner 51:303–308

Deer WA, Howie RA, Zussman J (2013) An introduction to the rock-forming minerals, 3rd edn. Mineralogical society, London

Dixon JB (1989) Kaolin and serpentine group minerals. In: Dixon JB, Weed SB (eds) (Co-eds) minerals in soil environments, 2nd edn. Soil Science Society of America, Madison, pp 467–525

Dixon JB, Schulze DG (eds) (2002) Soil mineralogy with environmental applications. SSSA book series, no. 7. SSSA, Madison

Dixon JB, Weed SB (eds) (1989) Minerals in soil environment. SSSA book series no. 1. SSSA, Madison

Egashira K, Ohtsubo M (1983) Swelling and mineralogy of smectites in paddy soils derived from marine alluvium, Japan. Geoderma 29:119–127

Greene-Kelly R (1955) Dehydration of montmorillonite minerals. Mineral Mag 30:604–615

Harris W, White GN (2008) X-ray diffraction techniques for soil mineral Identification. In: Ulery A, Vepraskas M, Wilding L (eds) Methods of soil analysis. Part 5. Mineralogical methods. SSSA book series, no. 5. SSSA, Madison, pp 81–115

Higashino T (1990) The higher grade metamorphic zonation of the Sambagawa metamorphic belt in central Shikoku. Japan J Metam Geol 8:413–423

Hsu PH (1989) Aluminum hydroxides and oxyhydroxides. In: Dixon JB, Weed SB (eds) (Co-eds) Minerals in soil environments, 2nd edn. Soil Science Society of America, Madison, pp 331–378

Joussein E, Petit S, Churchman J, Theng B, Righi D, Delvaux B (2005) Halloysite clay minerals – a review. Clay Miner 40:383–426

Kampf N, Scheinorst AC, Schulze DG (2012) Oxide minerals in soils. In: Huang PM, Li Y, Sumner ME (eds) Handbook of soil sciences, properties and processes, vol 22, 2nd edn. CRC Press/Taylor & Francis Group, Boca Raton/London/New York, pp 1–34

Kodama H (2012) Phyllosilicates. In: Huang PM, Li Y, Sumner ME (eds) Handbook of soil sciences, properties and processes, vol 21, 2nd edn. CRC Press, Taylor & Francis group, Boca Raton/London/New York, pp 1–49

Malla PB, Douglas LA (1987) Problems in identification of montmorillonite and beidellite. Clay Clay Miner 35:232–236

McKenzie RM (1989) Manganese oxides and hydroxides. In: Dixon JB, Weed SB (eds) (Co-eds) Minerals in soil environments, 2nd edn. Soil Science Society of America, Madison, pp 439–465

Molloy MW, Kerr PF (1961) Diffractometer patterns of A.P.I. reference clay minerals. Am Mineral 46:583–605

Nanzyo M, Tsuzuki H, Otuska H, Yamasaki S (2001) Origin of clay-size vermiculite in sandy volcanic ash soils derived from modern Pinatubo lahar deposits in Central Luzon, Philippines. Clay Sci 11:381–390

Soil Survey Staff (1999) Soil taxonomy, a basic system of soil classification of making and interpreting soils surveys, USDA-NRCS, agriculture handbook no. 436, U.S. Government Printing Office, Washington DC

Sudo T, Shimoda S (1978) Clays and clay minerals of Japan. Developments in sedimentology 26, Elsevier, Amsterdam coprinted by Kodansha LTD., Tokyo, pp 1–326

Taguchi T, Enami M (2014) Compositional zoning and inclusion of garnet in Sanbagawa metapelites from the Asemi-gawa route, central Shikoku. Japan J Mineral Petrol Sci 109:1–12

Tokashiki Y, Hentona T, Shimo M, Arachchi LPV (2003) Improvement of the successive selective dissolution procedure for the separation of birnessite, lithiophorite, and goethite in soil manganese nodules. Soil Sci Soc Am J 67:837–843

Wada K, Aomine S (1966) Occurrence of gibbsite in weathering of volcanic materials at Kuroishbaru, Kumamoto. Soil Sci Plant Nutr 12:151–157